Journal Pre-proof

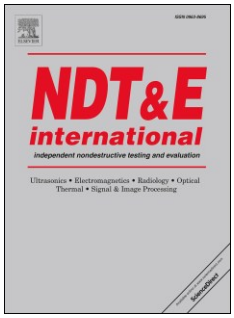

Enhancement of microwave time reversal imaging using metallic reflectors

Saptarshi Mukherjee, Xiaodong Shi, Srijan Datta, Yiming Deng, Satish Udpa, Lalita Udpa

PII: S0963-8695(19)30271-3

DOI: https://doi.org/10.1016/j.ndteint.2019.102192 Reference: JNDT 102192

To appear in: *NDT and E International*

Received Date: 14 May 2019

Revised Date: 1 November 2019

Accepted Date: 8 November 2019

Please cite this article as: Mukherjee S, Shi X, Datta S, Deng Y, Udpa S, Udpa L, Enhancement of microwave time reversal imaging using metallic reflectors, *NDT and E International* (2019), doi: https://doi.org/10.1016/j.ndteint.2019.102192.

This is a PDF file of an article that has undergone enhancements after acceptance, such as the addition of a cover page and metadata, and formatting for readability, but it is not yet the definitive version of record. This version will undergo additional copyediting, typesetting and review before it is published in its final form, but we are providing this version to give early visibility of the article. Please note that, during the production process, errors may be discovered which could affect the content, and all legal disclaimers that apply to the journal pertain.

© 2019 Published by Elsevier Ltd.

Journal Pre-proof

Enhancement of microwave time reversal imaging using metallic reflectors

Saptarshi Mukherjee[1a], Xiaodong Shi[b], Srijan Datta[b], Yiming Deng[b], Satish Udpa[b], Lalita Udpa[b]

[a]Lawrence Livermore National Laboratory, California 95035, USA [b]Nondestructive Evaluation Laboratory, Michigan State University, East Lansing, Michigan 48824,USA

Abstract

Thereisagrowinginterestintheuseofcompositesinseveralindustriessuchasaerospace, automotiveandcivilinfrastructureduetotheiruniquepropertiessuchaslight-weight, corrosionresistanceandexcellentthermo-mechanicalproperties.However,itiscriticalto ensure that no defects, such as disbonds, voids and delaminations are introduced during fabrication or during service. A variety of nondestructive evaluation (NDE) techniques have been proposed and developed to detect such defects that can compromise the integrity of these structures. Microwave NDE techniques are well suited for inspection of dielectric materials such as composites because of the ability of electromagnetic waves to interact with these materials. Far field electromagnetic inspection systems have the capability of rapid, large area inspection at large stand-off distance. However the diffraction limits restrict the resolution of conventional far field imaging. This contribution focuses on enhancing the resolution of microwave far field imaging using metal reflectors to increase the virtual aperture of the receiver array. Model based studies demonstrate the feasibility and robustness of this approach and also determine the limits of this technique. Preliminary experimental results based on a time reversal cavity environment validates the approach for enhancing the resolution of microwave NDE imaging.

Keywords: Microwave imaging, Nondestructive Evaluation, Composite Materials

1. Introduction

Composites are being increasingly used in several industries to replace metals, fully or partially due to their unique properties such as high strength, durability and light-weight [1]. They also offer flexibility and strategic tailoring of their mechanical properties. Defects such as disbonds, voids, delaminations may be formed during the manufacturing as well as in-service stages of these structures [2]. These defects affect the overall structural strength, performance and integrity resulting in catastrophic failure [3]. Thus, there is a need for a reliable nondestructive evaluation (NDE) system that can be utilized to rapidly inspect large areas of composites, and accurately detect potential anomalies [4, 5].

Journal Pre-proof

Currently ultrasonics, eddy current, X-ray, infrared thermography and optical imaging are some of the most widely investigated industrial NDE techniques [6, 7, 8]. Microwave NDE is a relatively new technique, particularly suited for lowloss and lossless

dielectric materials [9]. Since electromagnetic (EM) waves can penetrate such materials, the scattered fields contain valuable information about structural integrity of such materials. Some of the recent applications of Microwave NDE are corrosion detection in painted aluminum and steel substrates, flaw detection in Sprayed on Foam Insulation (SOFI) of space shuttles, disbond detection in CFRP strengthened cement based structures [10].

Microwave far field imaging techniques are particularly suited to image source, scatterers and anomalies in dielectric materials [11]. Microwave time reversal (MTR) is a source focusing method which can be utilized to image defects that act as secondary sources in composite materials [12]. The basic idea of MTR is that EM field components diverging out from a point source can be reversed in time and back-propagated in a numerical model to focus back at the original source location [13]. Introduced by Mathias Fink in 1992 for lithotripsy applications [14], TR was extended to EM waves by Lerosey et al. [15]. EM TR is now used widely in radar detection, breast tumor imaging and wireless charging applications [16, 17]. Some of the advantages of using TR over conventional tomographic imaging include its ease of implementation, non-iterative, quasi real-time nature, super-resolution and selective focusing capabilities [18]. However the diffraction limits restrict the resolution of conventional far field imaging [19]. Objects smaller than the operating wavelength are not detectable in far field microwave data. While near field imaging techniques provide much higher resolution, the scanning time can be very high for large areas [20]. Enhancing the imaging resolution for TR was first demonstrated for acoustic fields in the presence of a medium with random inhomogeneities [21]. The presence of random inhomogeneities produces multipath scattering of the acoustic wave, which enlarges the aperture of the receiver array than its actual physical size [22]. The same concept was extended to electromagnetics by Yavuz et al. in 2005 [23]. A similar multi-path scattering effect is observed due to multi-path reflection of EM waves in the presence of metals, in contrast to ultrasonic waves which do not exhibit such a behavior as they can propagate through metals [24]. Numerical studies have shown the application of metal confinement to enhance the focusing effect [25]. However, the application of such metallic reflectors for improving imaging resolution and its extension to NDE experiments have not been accomplished to the best of the authors' knowledge. This paper focuses on enhancing the resolution of far field microwave NDE by using metal reflectors to increase the virtual aperture size.

The reflectors serve to reflect the outgoing EM fields and directs them towards the receiving antenna array. The increase in the aperture size of the receiving antenna array due to the reflected energy results in an increase in the spatial resolution. Simulation studies and parameteric analysis demonstrate the capability and robustness of the approach for imaging disbonds in metal-composite joints. Experimental studies involving source localization and disbond detection in a test setup with and without metal reflectors validate the proposed approach.

Journal Pre-proof

The paper is organized as follows. Section 2 describes the TR algorithm and describes simulation studies related to the first approach. Accurate results and high imaging quality achieved from the parametric limits obtained from simulation studies demonstrate the efficacy of the approach. In section 3, experimental studies are conducted with the help of a time-domain laboratory setup and a TR back-propagation code for high resolution imaging of external source as well as defects in composites.

2. TR imaging

TR is a consequence of the wave reciprocity property. The scalar wave equation in a lossless medium is given by [26]

$$\left(\nabla^2 - \frac{n^2(r)}{c^2}\frac{\partial^2}{\partial t^2}\right)\varphi(r,t) = 0 \quad (1)$$

Since the above EM wave equation is time-symmetric, the above equation yields a diverging, causal solution $\phi(r,t)$ and a converging, anti-causal solution $\phi(r,-t)$. Due to this property, the scattered fields from a point source collected by the receiver antenna array can be time reversed and back propagated using a numerical model to focus back at the source location.

2.1. TR algorithm

The TR algorithm can be adapted for NDE applications for imaging defects in dielectric materials, as outlined below [27].

1. an ultra-wide band pulse is transmitted from a source antenna to the sample;
2. scattered signals due to the defective sample and healthy sample are measured byreceivers placed at separate locations and subtracted to obtain the perturbation signal;
3. the perturbation signal waveform is reversed in time and back propagated throughthe healthy sample using a numerical model;
4. localization techniques are applied to obtain spatio-temporal focusing and imagingof defects in the sample.

The wave propagation phenomenon is numerically modeled for a two-dimensional TMz mode excitation using the finite difference time domain technique (FDTD), with convolution perfectly matched layer (CPML) boundary conditions to truncate the computational domain. The FDTD parameters satisfy Courant's stability criterion and are defined as follows: $\Delta x = \Delta y = \lambda/10, \Delta t = \Delta x/2c$, where $\Delta x, \Delta y$ and Δt are the FDTD cell sizes and time steps respectively [28]. The transmitter is modeled as a point source, and a circular array of sensors is used to collect the back-scattered fields. The fields are time reversed and back propagated in the same model. A time integrated energy localization method is utilized to detect presence of defects in the dielectric material. Simulation results and parametric analysis have been conducted as part of prior research and have helped us determine the feasibility and limits of the parameters that affect the TR algorithm [12]. These parameters are used for conducting passive TR experiments to image defects in composite materials.

2.2. High resolution focusing with metal reflectors

The electric field radiated from the point source propagating towards the receivers can be expressed in a cylindrical coordinate system as

$$E_z(\omega,\rho) = -\frac{j}{4}E_0(\omega)H_0^{(2)}(k\rho), \tag{2}$$

where $E_0(\omega)$ is the electric field magnitude, ω is the frequency of the wave, k is the wave vector, ρ is the distance between the source and observation point and $H_0^{(2)}(k\rho)$ is the second order Hankel function describing the outgoing propagating wave. Thus the fields measured by the receiver array can be expressed as

$$E_z^i(\omega,\rho) = E_z(\omega,\rho_i) \tag{3}$$

where i is the receiver antenna, ρ_i denotes the position of the ith receiver antenna and $i\epsilon[1,N]$ where N is the total number of antennas of the array.

The cross range (Δ_c) and down range resolution (Δ_d) for TR is given by

$$\Delta_c = \lambda\left(\frac{l}{a}\right), \qquad \Delta_d = \lambda\left(\frac{l}{a}\right)^2, \tag{4}$$

where l and a are the distance of source from the receiver array and receiver aperture length respectively. The presence of the metal reflectors in effect extends the aperture of the receiver array. This can be physically understood from the following argument. The metal reflectors behave like additional receivers that trap waves that would have otherwise diverged away from the receiver array, thereby virtually extending the effective aperture size (a_e). The relationship between the new aperture size and the geometrical parameters of the configuration shown in Figure 1 can be derived using trigonometric identities as follows.

$$\rho_n = \frac{y_n}{cos\theta_N}; \qquad \theta_N = \tan^{-1}\left|\frac{x_n}{y_n}\right|;$$

$$\rho_n^{'} = \frac{y_n}{cos\theta_N^{'}} \quad ; \quad \theta_N^{'} = \tan^{-1}\left|\frac{x_m}{y_n}\right|; \quad \theta_N^{"} = \tan^{-1}\left|\frac{d+x_m}{y_n}\right| \quad ; \quad \frac{d}{d+x_m} = \frac{y_n - y_m}{y_n} \quad ; \tag{5}$$

Figure 1: Configuration with ray diagram with metal reflectors

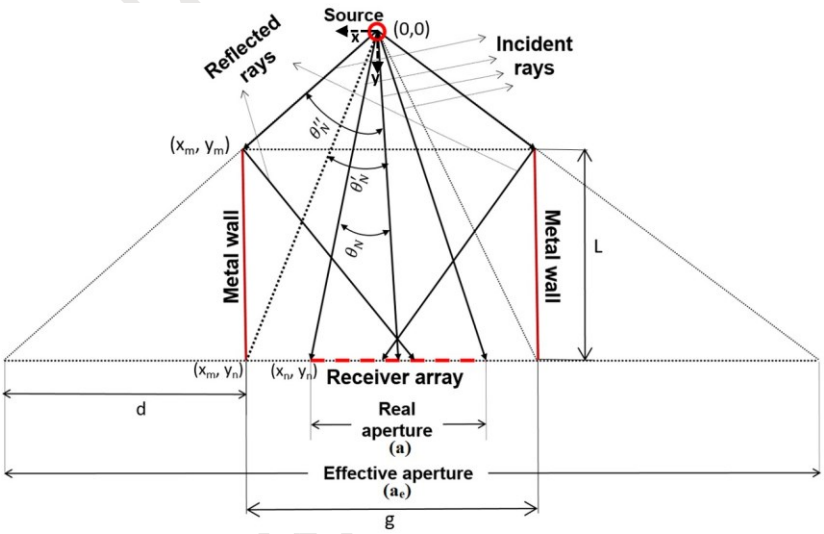

Table 1: Materal Properties

Material	**Relative Permittivity**	**Loss Tangent**	**Spatial dimensions** (m×m)
GFRP	3.8	0.017	0.6×0.1
Epoxy	3.6	0.032	0.6×0.02
Disbond	1	0	varying

where d is half of the increase in the aperture size. Combining the two equations of (5) we obtain,

$$\theta_N'' = \tan^{-1}\frac{x_m}{y_m} \quad (6)$$

In practically all the cases, $d > 0$, leading to $\theta_N'' > \theta_N$ leading to the extended aperture size and hence an improvement in the imaging resolution.

2.3. Numerical validation

Numerical studies were conducted with and without the metal reflectors in order to study the effects of the reflectors on imaging resolution.

2.3.1. Source focusing

The schematic for the simulation is shown in Fig. 2 (a). 50 receivers are placed over an aperture size of 70 cm, at a distance of 70 cm away from the source. The fields radiated from the point source are received by the receiver array, time reversed and back-propagated in the model in accordance with the time reversal algorithm. The time integrated back-propagated energy image without the metal reflectors is shown in Fig. 2 (b). Next, metal reflectors are introduced to the left and right of the source and their effect on resolution is studied using the simulation model. The length of the metal and spacing between metals are denoted as L and g respectively. Two cases, namely (i) g=20cm, L=40cm and (ii) g=40cm, L=70 cm are investigated. The corresponding time integrated energy image for the two cases are shown in Figs. 2 (c, d). It is seen from Fig. 2 (c) that the focusing resolution is improved and images show a tighter focal spot, with relatively better down range resolutions. In accordance with (6), the resolution is further improved when d and l are increased due to an increase in effective receiver aperture size as seen in Fig. 2 (d).

2.3.2. NDE of metal-composite joints

Next, a test sample comprising metal-composite joint is introduced in the inspection geometry shown in Fig. 3 (a). schematic of the simulation is shown in Fig. 3 (a). The geometry of the problem consists of a Glass Fiber Reinforced Polymer (GFRP) composite material adhesively bonded to a metal layer (conductor) via an epoxy layer. Defects in the form of disbonds are introduced as air gaps in the epoxy layer. The material properties and spatial dimensions of the sample are summarized in Table 1. The scattered signals are subtracted from a baseline measurement to obtain the defect contribution.

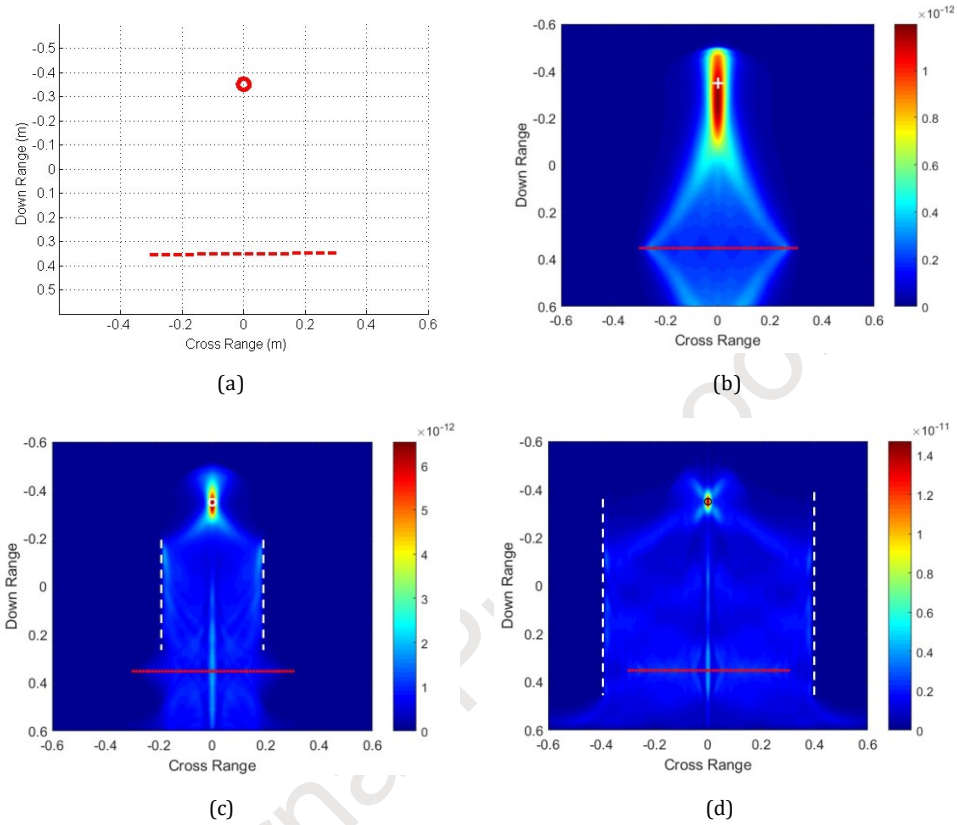

Figure 2: Source focusing (a) Schematic of test geometry, (b) TR energy without metal reflectors, (c) TR energy with metal reflectors, (d) TR energy with wider coverage of metal reflectors

The defect signals are time reversed and back-propagated in accordance with the time reversal algorithm. The back-propagated time reversed energy highlights the location and spatial extents of the disbond, as seen in Fig.. 3 (b). However, there is a spreading effect observed along the down range direction resulting in a smeared image of the defect, due to limited aperture size of the receiver array along the down range direction. Next, simulations are carried out with metal reflectors with g= 20 cm and L= 17 cm. As in the case of source focusing results, the TR energy is more accurately focused near the disbond location when the metal reflectors are introduced. The down range spreading effect is diminished to a large extent with the metal reflectors, leading to an enhancement in imaging resolution. The cross range signal is defined by a line scan across the energy image corresponding to the source location. There is also improvement in the cross range resolution as can be seen from the comparison of the cross range signals with and without the metal reflectors (Fig.3 (d)). The full width at half maxima (FWHM) of the signals is used to estimate the length of the disbond. The true disbond length is 3 cm; the estimated length without the metal reflectors is 7.5 cm and in the presence of the metal reflectors, the

estimate is 4cm. This example quantitatively validates the hypothesis of enhancing imaging resolution via increased aperture size by introducing appropriate metal reflectors.

2.4. Parametric analysis

Parametric studies are conducted with respect to the metal reflector lengths and location in order to understand the effect of these parameters on the TR energy and determine the robustness of the approach. For each of these parameters, the full width at half maxima value of the time-reversed energy was examined, and used as the quantitative can also be utilized to estimate the bounds on accuracy for different test geometries. metricforperformanceevaluation.Theparameterlimitsobtainedfromthesimulations

2.4.1.Metallength

Simulationstudiesareconductedwithsimilarconfiguration,asshowninFig.3(a) andthemetallengthisvariedfrom5cmto40cm,withafixedspacingof80cm. Simulationsareperformedconsideringtwodisbonds,eachoflength3cmlocatedwith aspacingof20cm.Fromtherelationshipderivedin(6),weobservethatas $Y_m \rightarrow 0$,

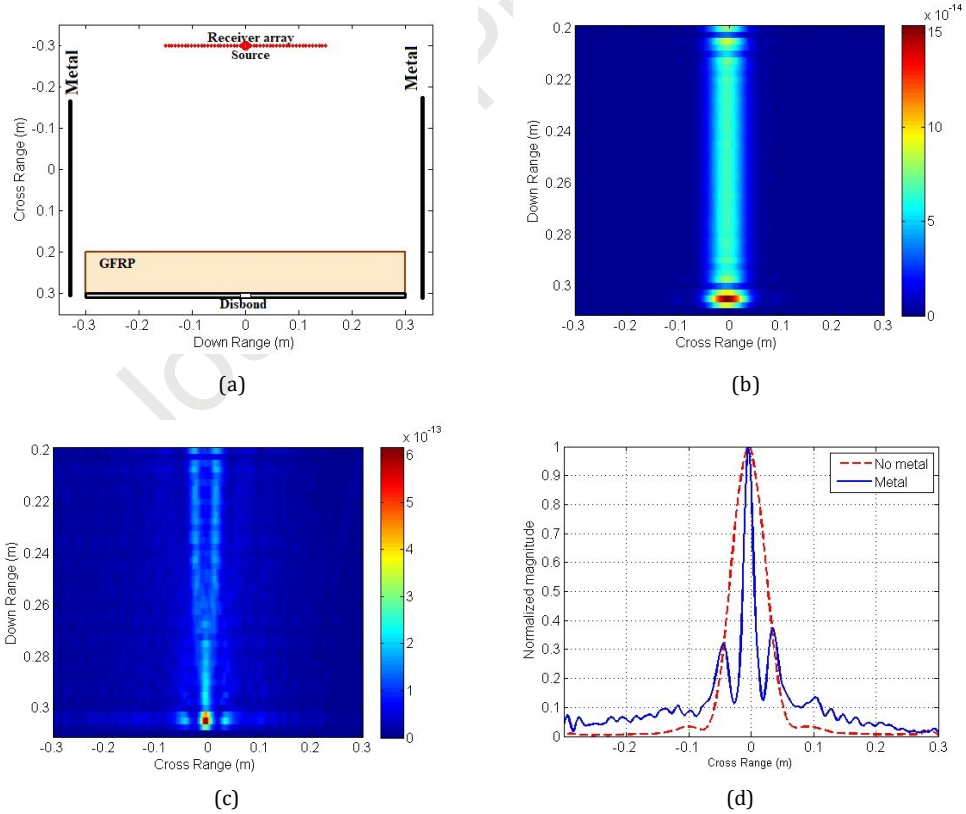

Figure 3: Detection of disbonds (a) Schematic of test geometry, (b) TR energy without metal reflectors,

(c) TR energy with metal reflectors, (d) Comparison of cross range signals

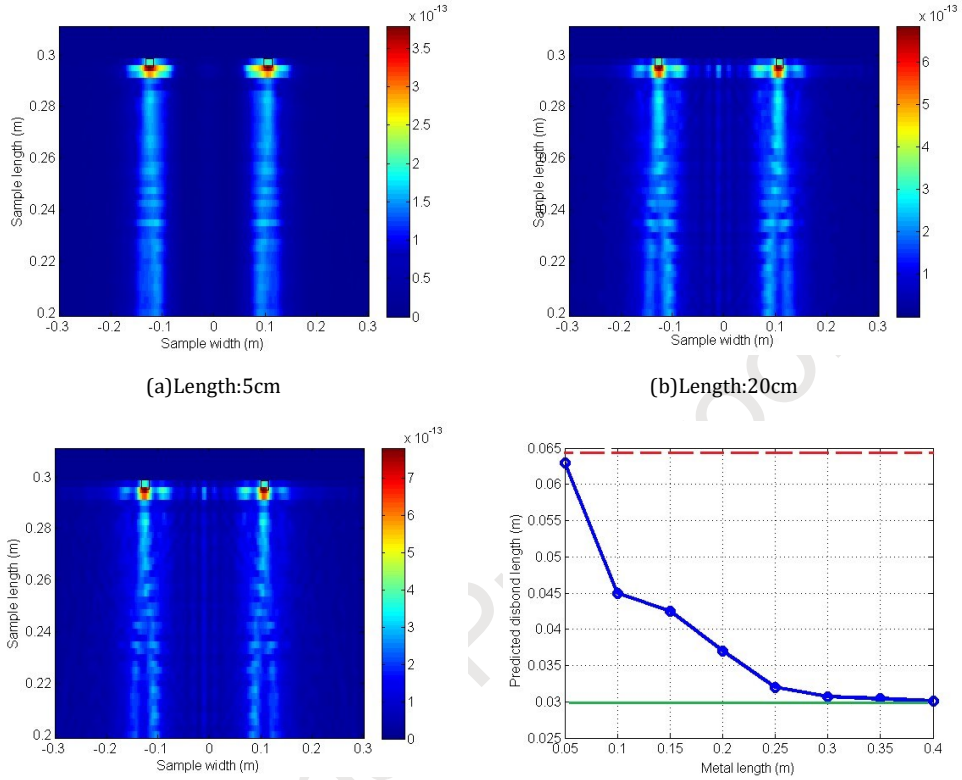

(a)Length:5cm (b)Length:20cm

(c) Length : 40 cm (d)

Figure 4: (a, b, c) TR energy for varying metal lengths, (d) Parametric analysis of width of predicted disbond vs metal lengths (green solid line denotes actual disbond length, red dashed line denotes predicted disbond length without metal)

$\theta_N^0 \rightarrow (-\pi/2, \pi/2)$, which is the resolution obtained without the metal reflectors. As $Y_m \rightarrow Y_n$, $\theta_N' \rightarrow \theta_N$). As the length of the metallic reflectors increase, the incident field at larger angles get reflected towards the receiver array, leading to an improvement in resolution. As $Y_m \rightarrow Y_\infty$, $\theta_N' \rightarrow (-2\pi, 2\pi)$. With an infinitely long metal plate, incident field at all angles are received by the receiver array, leading to a best possible resolution of $\Delta_c = \lambda/(2\pi)$ and $\Delta_d = \lambda/(2\pi)^2$. The time reversed energy images for lengths of 5 cm, 20 cm and 40 cm respectively are shown in Figs.4 (a-c). It can be seen that the imaging resolution improves with increase in the length of the metal reflectors. The relationship between the estimated disbond length with the metal length is plotted in Fig.4 (d). It is seen that the estimation of the disbond size becomes more accurate with increase in the length of the reflectors, the estimated value nearing its actual value when the metal length is 40 cm.

2.4.2. Spacing between metals

Simulation studies are conducted with the previously mentioned configuration and the spacing between metals is varied from 6 cm to 8.2 cm, with their lengths fixed at

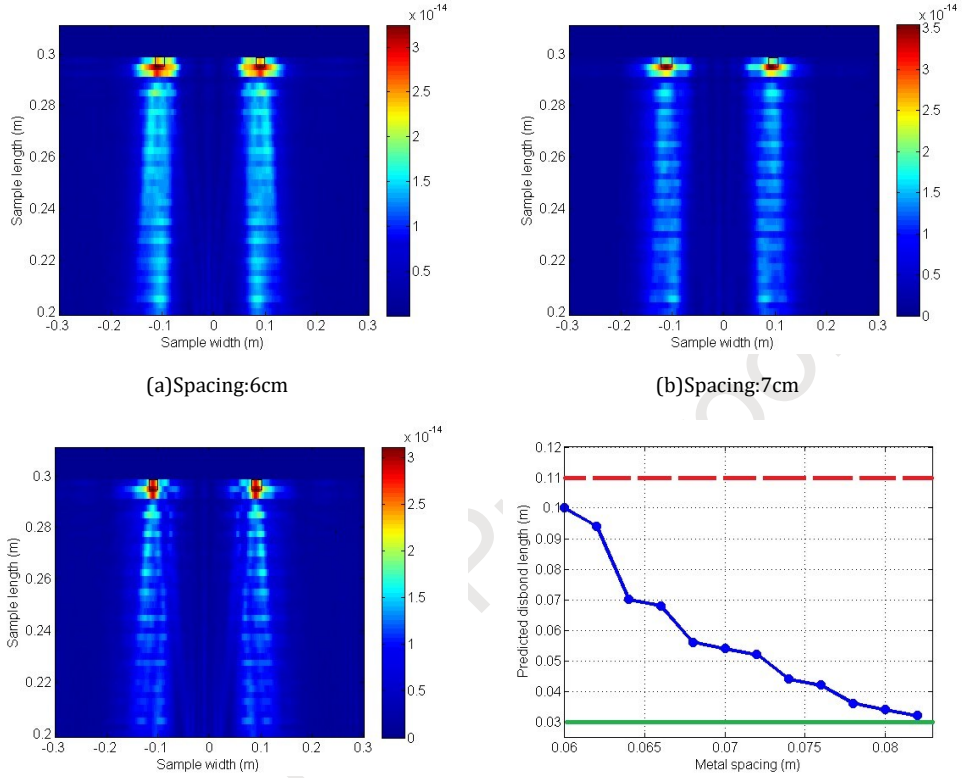

(a)Spacing:6cm (b)Spacing:7cm

(c) Spacing: 8 cm (d)

Figure 5: (a, b, c) TR energy for varying metal spacing, (d) Parametric analysis of width of predicted disbond vs metal separation (green solid line denotes actual disbond length, red dashed line denotes predicted disbond length without metal)

50 cm. From the relationship derived in (6), we observe that as $x_N \to 0,\ \theta'_N \to 0$. As $x_n \to (y_n - Y_M),\ \theta_N \to \pi/4$. As the spacing between the metallic increase, the incident field at larger angles get reflected towards the receiver array, leading to an improvement in resolution. As $x_n \to \infty,\ \theta'_N \to (-2\pi, 2\pi)$. With a metal plate placed infinitely far away from the excitation source, incident field at all angles are received by the receiver array, leading to a best possible resolution of $\Delta_c = \lambda/(2\pi)$ and $\Delta_d = \lambda/(2\pi)^2$. The time reversed energy images for spacing of 6 cm, 7 cm and 8 cm are shown in Figs.5 (a-c) respectively. It is seen that the imaging resolution improves with increase in the length of the metal reflectors. The relationship between the estimated disbond length with different spacing is plotted in Fig.5 (d). It is seen that the estimation of the disbond size becomes more accurate with increase in the metal spacing, the estimated value nearing its actual value when the

metal spacing is 8.2 cm. This is consistent with the mathematical relationship mentioned earlier.

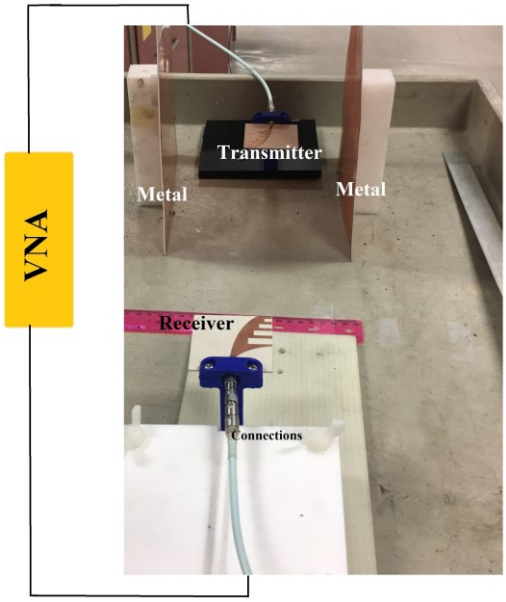

Figure6:Experimentalsetup

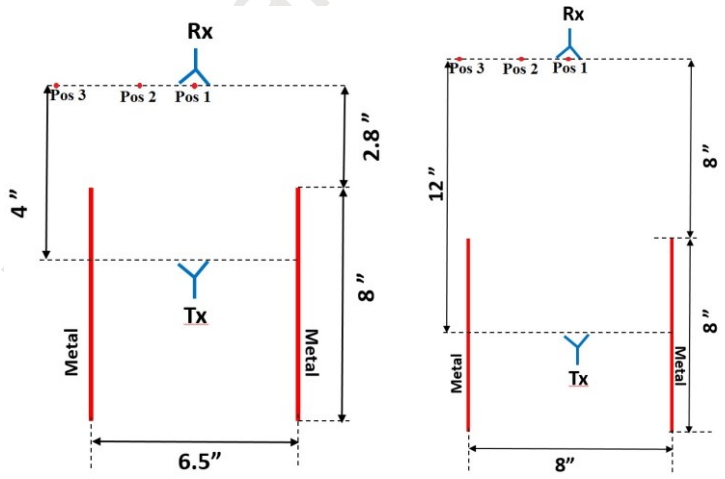

Figure 7: Experimental configurations along with dimensions: (a) Configuration 1, (b) Configuration 2

3. Experimental studies

Experimental studies are performed with an ultra-wide band frequency domain setup and metal reflectors. The effect of the metal walls on the resolution of the time reversed image is demonstrated experimentally.

3.1. Experimental setup

The experimental setup is shown in Fig. 6 (a). Two vivaldi antennas are used as ultrawide band transmitting and receiving antennas, operating between 3 and 10 GHz. The wide bandwidth of the antenna results in a narrow pulse width, which leads to a higher range resolution of the imaging system[29]. The performance of the vivaldi antenna has been discussed in details as part of a previous research [30]. The antennas are probed with the help of a E5070B Vector Network Analyzer (VNA). The metal reflectors are placed in between the transmitter and receiver antenna similar to the simulation schematics discussed before. The receiver antenna is moved linearly in order to emulate the receiver array. Scattering parameters are measured while moving the receiver antenna.

3.2. Source localization

Two different configurations with varying distances between the transmitter and receiver and metal spacing are used for performing the experiments. The schematic along with the exact dimensions used for obtaining the measurements for both configurations are shown in Fig. 7. Measurements are taken with and without the metal reflectors. The wide-band insertion loss S_{12} magnitude and phase data measured over the frequency range, which measures the power received from the transmitter to the receiver with and without the metal reflectors for three different receiver antenna positions marked in Fig. 7 are shown in Figs. 8 (a-f) respectively. It is observed that both amplitude and phase measurements are distinct for the three positions. The measurements show consistent change in both amplitude and phase throughout the frequency range, which is crucial for TR in order to ensure that the pulse delay and attenuation between corresponding antenna measurements are preserved. The measurements for the metal configuration 2 are smoother than the other configurations due to the finer frequency sampling and more distance between the transmitter and receiver antenna. However, we will observe later that this factor does not hamper the TR imaging quality.

3.2.1. Experimental results

The time domain pulses are generated from the wide-band frequency domain data by a series of operations involving windowing the frequency domain data to reduce clutter, followed by conversion to time domain by inverse fourier transform operation. The obtained pulses are time gated to eliminate background reflections and fed to the time reversal algorithm for back-propagation. The time domain pulses with and without the metal reflectors received by the antenna array are shown in Fig. 9. In the absence of the metal reflectors, the direct fields from the transmitter reach the receivers, as shown in Fig. 9 (a). Additonally, there is some distortion in the pulse at later time intervals, possibly due to surrounding clutter and finite frequency sampling measurements. However, time gating of these pulses can eliminate such distortions. In the presence of the metal reflectors, the pulse comprises direct fields from the transmitter as well as fields reflected by the metal boundaries. However for metal configuration 1, the maximum time delay between the

Journal Pre-proof

direct and reflected ray paths (0.15 ns) is less than the pulse width (0.20 ns). Hence it is hard to separate out the two components from the resultant pulse, as shown in Fig. 9 (b). For metal configuration 2, the time delay between the direct and reflected ray paths (0.25 ns) is almost equal to the pulse width . Hence it is barely able to distinguish between the two components from the resultant pulse, as shown in Fig. 9
(c).

The pulses are fed through the time reversal algorithm for back-propagation and the time reversed energy is plotted in order to perform source localization. The time reversed energy without the metal reflector is shown in Fig. 10 (a). Most of the energy is focused around the receiver array region, with a weak focusing observed around the source

rnal Pre-

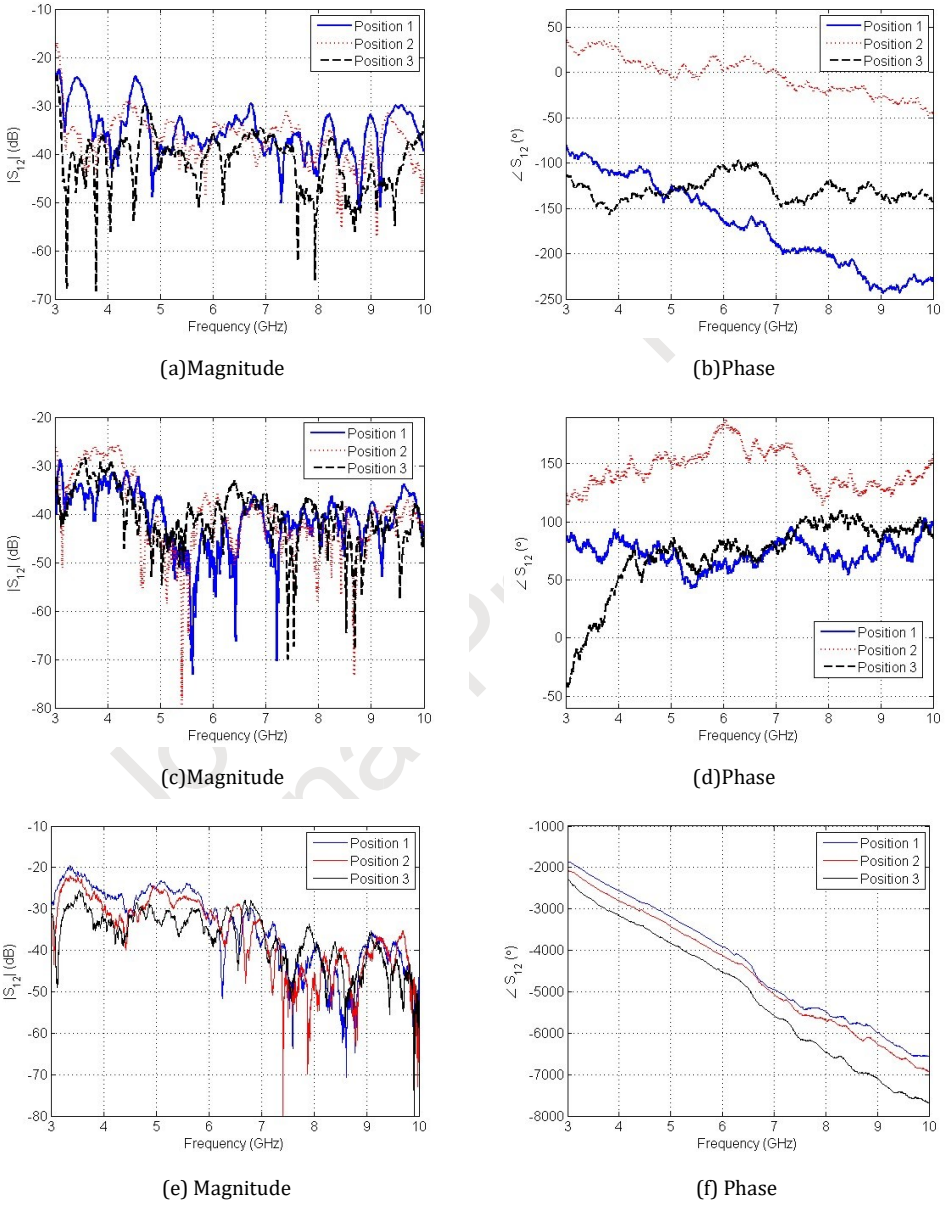

(a)Magnitude (b)Phase

(c)Magnitude (d)Phase

(e) Magnitude (f) Phase

Figure 8: (a, b) S_{12} with no metal, (c, d) S_{12} with metal configuration 1, (e, f) S_{12} with metal configuration 2

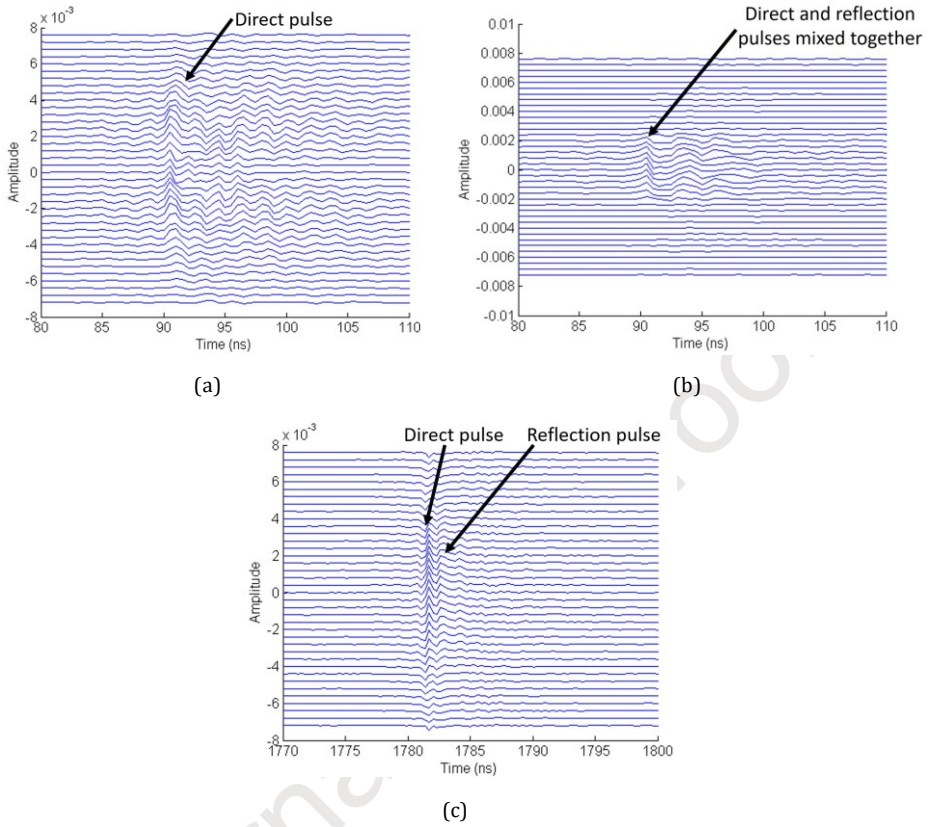

Figure 9: (a) Pulse with no metal, (b) Pulse with metal configuration 1, (c) Pulse with metal configuration 2

antenna. The focal spot around the source is stretched out both in down range and cross range directions. In the absence of metal reflectors, most of the fields diverging away from the source are not detected by the receiver array, thus leading to weak detection of the source. Next, the metal reflectors are introduced according to configuration 1 (Fig. 7 (b)). TR is performed with the pulses obtained from the system. Although some of the energy is focused around the reciever array, the source can be clearly detected in this case, with a relatively sharper focal spot. The metal reflectors behave like additional receivers that trap waves that would have otherwise diverged away from the receiver array, thus virtually extending the effective receiver array aperture and enhancing the imaging quality. However, it is also observed that bulk of the energy is focused at the metal reflectors, especially at the region between the receiver array and the reflectors due to the strong interactions between fields radiating out from the receiver and reflections from the metal reflector. In order to eliminate these additional artifacts, a new configuration is utilized with the spacing between the metal increased from 6.5 inches to 8 inches and the distance between the transmitter antenna and the receiver antenna array increased from 4 inches to 12 inches (Fig. 7 (b)). As shown in Fig. 10 (c), the TR energy for this configuration is

primarily focused at the source location, with limited energy around the metal reflectors. Although some of the energy is focused at the center of the receiever array, it does not hamper the quality of the source localized image. Additionally, it is interesting to note that the focal spot is slightly stretched along both cross and down range directions. This is directly related to (4) explained before. The increase in distance between the transmitter and receiver (l) leads to a decrease in focal resolutions. A comparison of the cross range resolution can be obtained by plotting the TR cross range signals in Fig. 10 (d). It can be clearly observed that the focal spot is quite stretched withoutthemetalreflectors,whileitisquitefocusedwiththereflectorsalongthecross rangedirection.Althoughthefocusingissuperiorforconfiguration1,additionalartifacts andsidelobesduetothereceiverarraypositionedclosertothemetalandalessermetal spacingareobservedforthisconfigurationwhichhampertheoverallimagingquality.On thecontrary,theartifactsandsidelobesareeliminatedatthecostofarelativelypoor resolutionduetoanincreasedgapbetweenthetransmitterandthereceiverarray.

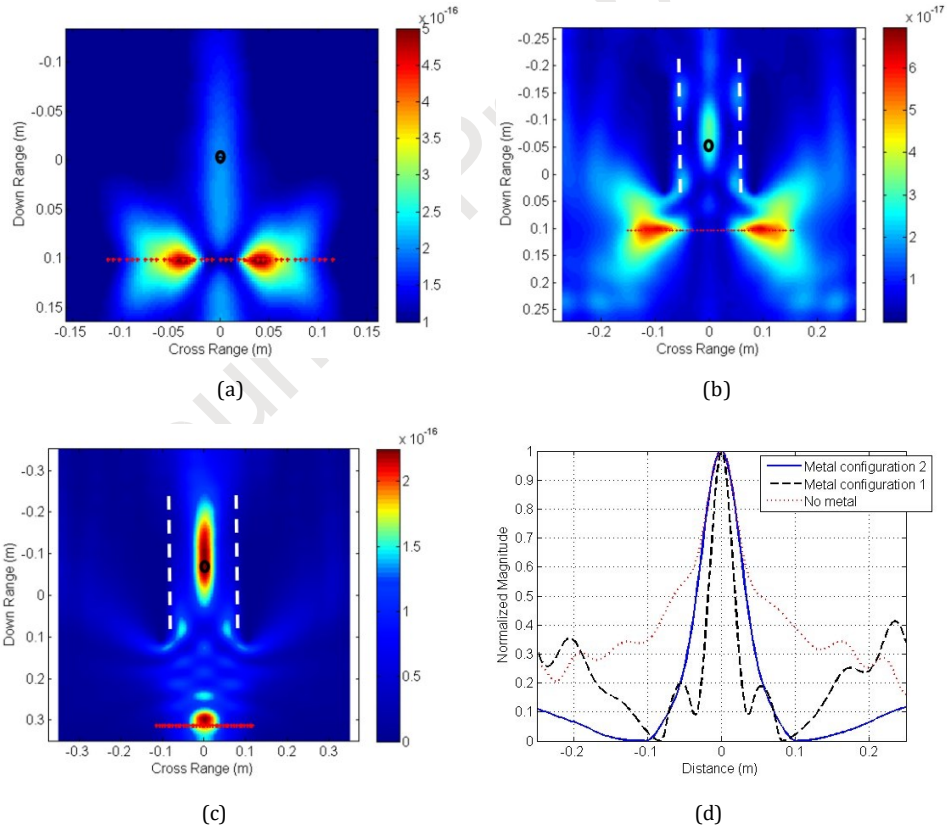

Figure 10: TR energy for source imaging (a) without metal, (b) with metal configuration 1, (c) with metal configuration 2, (d) Comparison of different configurations (white line indicates metal reflector and black circle indicates source location)

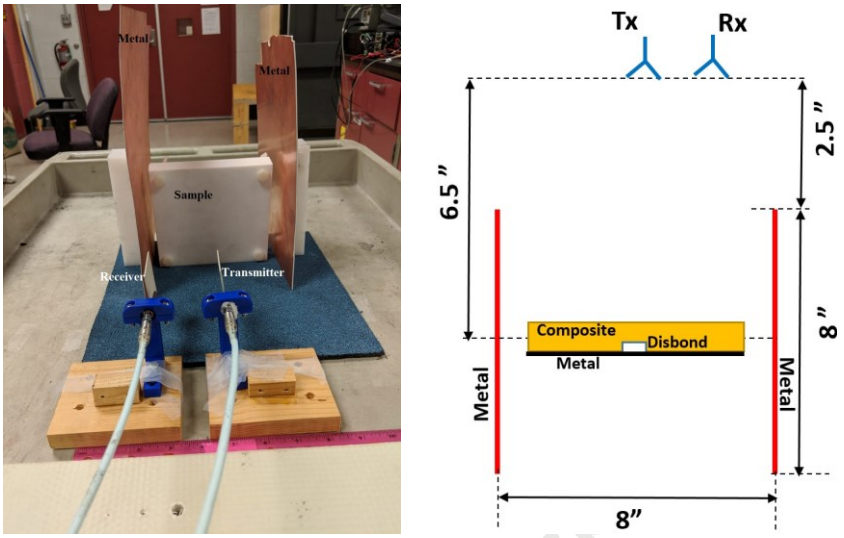

(a) (b)

Figure 11: NDE of metal composite joints: (a) Experimental setup, (b) Configuration

3.3. Disbond detection in composites

Finally, the experimental system is utilized with metal reflector and sample composed of a simulated metal composite joint. The sample is composed of a Teflon (ε_r = 2.1, tanδ=0.00028) square section of dimensions 150 mm × 150 mm and a thickness of 28 mm, bonded to an aluminum sheet by Teflon screws and bolts[12]. The disbond is created by machining a groove of dimensions 15 mm × 5 mm ($\lambda/2 \times \lambda/6$) at the metal dielectric interface along the entire length of the sample. The sample with the groove invariant along the z direction, closely resembles a 2-D metal-composite plane with a disbond, as shown from the top view of Figure **??** (b). In order to perform the baseline subtraction, an identical sample without a defect is used. As seen from the configuration in Fig. 11 (a), the sample is placed inside the metal boundaries, while keeping both transmitter and receiver outside. The schematic along with the exact dimensions used for obtaining the measurements is shown in Fig.11 (b).

Measurements are taken with and without the presence of the metal reflectors. The wide-band insertion loss S_{12} magnitude and phase data measured over the frequency range with and without the metal reflectors at the fixed receiver position shown in Fig. 11

(b) for both samples with and without disbond are shown in Figs. 12 (a-d) respectively.It is observed that the amplitude and phase for samples with and without disbond consistently vary throughout the frequency range. The phase shift for the sample with disbond

is slightly smaller compared to the sample without disbond. This is because the EM waves travel faster through the defect region due to higher phase velocity ($v_p = c/\sqrt{\varepsilon_r}$) and reaches the receiver antenna faster in comparison to the sample with disbond, leading to the phase

variation. Additionally, it is also observed that the differences in insertion loss between the samples with and without disbond are higher with metal reflectors than in free space, due to more information on the scattered fields in the reflector environment

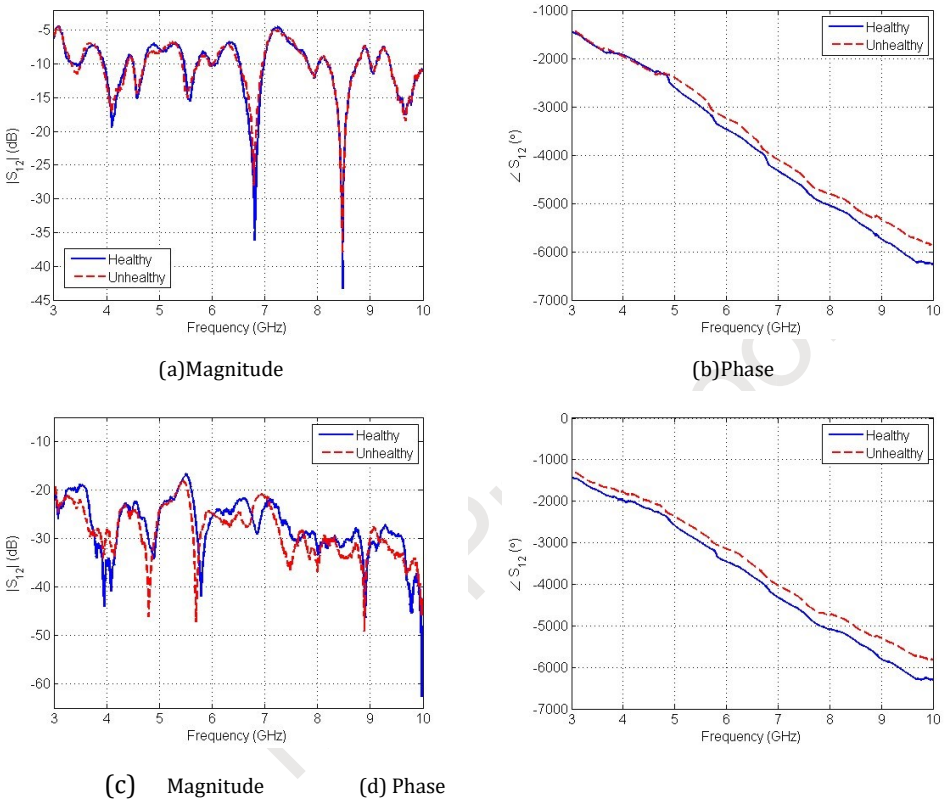

(a)Magnitude (b)Phase

(c) Magnitude (d) Phase

Figure 12: (a, b) S_{12} with no metal, (c, d) S_{12} with metal

as discussed before.

3.3.1 .Experimentalresults

The time domain pulses are generated from the wide-band frequency domain data with and without the metal reflectors. The defect contribution is obtained by subtracting the signals from samples with and without disbond. The pulses are fed through the time reversal algorithm for back-propagation in a healthy sample and the time reversed energy is plotted in order to perform source localization. The time reversed energy without the metal reflector is shown in Fig. 13 (a). It is observed that most of the energy is focused around the defect location. However, the focal spot around the defect is stretched out both in down range and cross range directions. In the absence of metal reflectors, most of the fields scattered by the disbond are not detected by the receiver array, thus leading to weak detection. Next, the metal reflectors are introduced according to Fig. 11 (b)). TR is

performed with the pulses obtained from the system. The time reversed energy with the metal reflector is shown in Fig. 13 (b). The back-propagated energy is focused around the defect location with an enhanced focusing around it. The focal spot around the defect is much more spatially confined than without metal reflectors. The metal reflectors behave like additional receivers that trap the field scattered from the defect

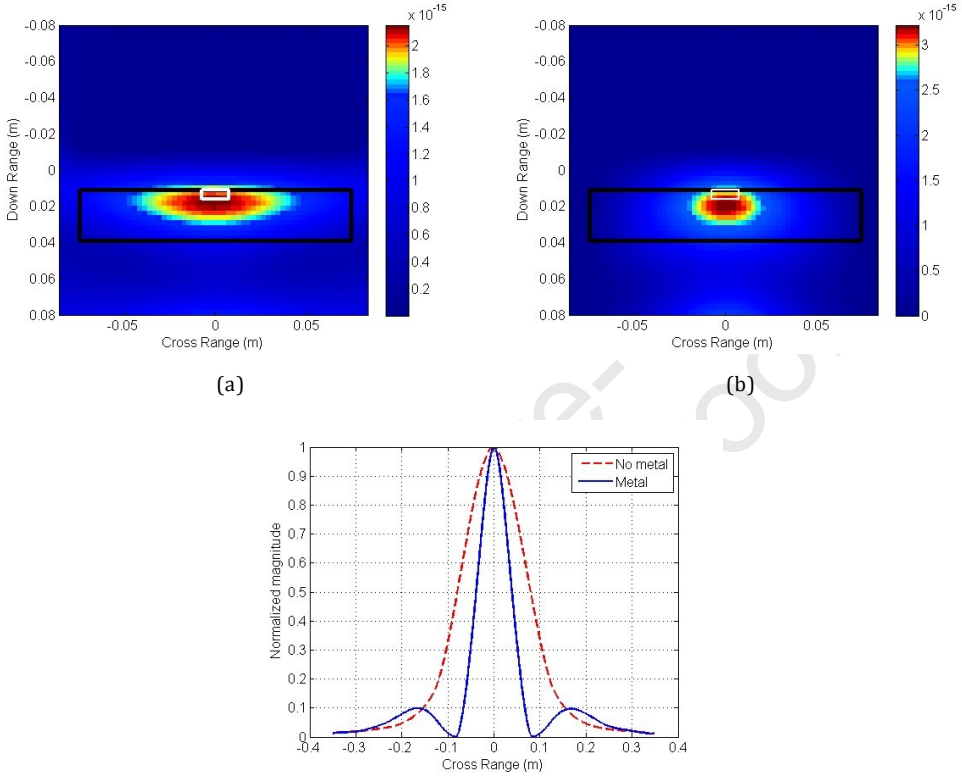

Figure 13: TR energy for defect imaging (a) without metal, (b) with metal, (c) with metal configuration 2, (d) Comparison of cross range signal

that would have otherwise diverged away from the receiver array, thus virtually extending the effective receiver array aperture and enhancing the imaging quality. The additional field information can also be observed from the higher value of the energy peak in the presence of the metal reflectors. A comparison of the cross range resolution can be obtained by plotting the TR cross range signals, corresponding to the defect location, as shown in Fig. 13 (c). It is observed that the focal spot is much more focused along the cross range direction with the metal reflectors than without them. The FWHM of the cross range signal is 5 cm and 10 cm with and without the metal reflectors, leading to a more accurate prediction with the metal reflectors. Experimental results on more realistic disbond (~ 0.5 mm) in GFRP composites will be performed as part of future research.

Journal Pre-proof

4. Conclusion

This research proposes a scheme for enhancing the resolution of microwave far field imaging by implementing time reversal imaging to data collected in the presence of metal reflectors. A mathematical analysis is performed to understand the effect of the metal reflectors on the imaging quality. Numerical studies show the feasibility of the approach for source focusing and defect detection. Parametric studies conducted with respect to the metal reflector properties provide some guidelines for choosing geometrical parameters of the test setup with metal reflectors. A frequency domain experimental setup based on a time reversal cavity environment is developed for performing experiments involving source localization and disbond detection in composites. Preliminary experimental results validates the approach for enhancing the resolution microwave NDE applications. Initial results demonstrate the efficiency of the methodology presented in this paper and lays the foundation for a robust, high resolution microwave imaging system for NDE of composites. Future work involves developing a 3-D back-propagation model that will be capable of detecting volumetric defects such as impact damages and delaminations in composite materials.

Acknowledgement

This work was supported by the National Science Foundation through Manufacturing USA program, award number 1762331.

References

[1] H. Ku, H. Wang, N. Pattarachaiyakoop, M. Trada, A review on the tensile properties of natural fiber reinforced polymer composites, Composites Part B: Engineering 42 (4) (2011) 856–873.
[2] B. Harris, Fatigue in composites: science and technology of the fatigue response of fibre-reinforced plastics, Woodhead Publishing, 2003.
[3] R. Kline, Nondestructive characterization of composite media, Routledge, 2017.
[4] D. E. Bray, R. K. Stanley, Nondestructive evaluation: a tool in design, manufacturing and service, CRC press, 1996.
[5] P. Banerjee, R. P. Palanisamy, L. Udpa, M. Haq, Y. Deng, Prognosis of fatigue induced stiffness degradation in gfrps using multi-modal nde data, Composite Structures 229 (2019) 111424.
[6] O. Karpenko, A. Khomenko, E. Koricho, M. Haq, L. Udpa, Monitoring of fatigue damage in composite lap-joints using guided waves and fbg sensors, in: AIP Conference Proceedings, Vol. 1706, AIP Publishing, 2016, p. 120005.
[7] G. Yang, A. Tamburrino, L. Udpa, S. S. Udpa, Z. Zeng, Y. Deng, P. Que, Pulsed eddy-current based giant magnetoresistive system for the inspection of aircraft structures, IEEE transactions on magnetics 46 (3) (2010) 910–917.
[8] P. Banerjee, O. Karpenko, L. Udpa, M. Haq, Y. Deng, Prediction of impact-damage growth in gfrp plates using particle filtering algorithm, Composite Structures.
[9] S. Kharkovsky, R. Zoughi, Microwave and millimeter wave nondestructive testing and evaluationoverview and recent advances, IEEE Instrumentation & Measurement Magazine 10 (2) (2007) 26–38.
[10] S. Bakhtiari, N. Qaddoumi, S. I. Ganchev, R. Zoughi, Microwave noncontact examination of disbond and thickness variation in stratified composite media, IEEE Transactions on Microwave Theory and Techniques 42 (3) (1994) 389–395.
[11] P. Roy Paladhi, A. Tayebi, P. Banerjee, L. Udpa, S. Udpa, Image reconstruction from highly sparse and limited angular diffraction tomography using compressed sensing approach, Progress In Electromagnetics Research 158 (2017) 21–36.

Journal Pre-proof

[12] S. Mukherjee, A. Tamburrino, M. Haq, S. Udpa, L. Udpa, Far field microwave nde of composite structures using time reversal mirror, NDT & E International 93 (2018) 7–17.
[13] M. Fink, Time reversal of ultrasonic fields. i. basic principles, IEEE Trans. Ultrason., Ferroelect., Freq. Control 39 (5) (1992) 555–566.
[14] M. Fink, D. Cassereau, A. Derode, C. Prada, P. Roux, M. Tanter, J.-l. Thomas, F. Wu, Timereversed acoustics, Rep. Prog. Phys. 63 (12) (2000) 1933.
[15] G. Lerosey, J. De Rosny, A. Tourin, A. Derode, G. Montaldo, M. Fink, Time reversal of electromagnetic waves, Phys. Rev. Lett. 92 (19) (2004) 193904.
[16] R. C. Qiu, C. Zhou, N. Guo, J. Q. Zhang, Time reversal with miso for ultrawideband communications: Experimental results, IEEE Antennas Wireless Propag. Lett. 5 (1) (2006) 269–273.
[17] P. Kosmas, C. Rappaport, Time reversal with the fdtd method for microwave breast cancer detection, IEEE Trans. Microw. Theory Techn. 53 (7) (2005) 2317–2323. doi:10.1109/TMTT.2005.850444.
[18] B. E. Henty, D. D. Stancil, Multipath-enabled super-resolution for rf and microwave communication using phase-conjugate arrays, Phys. Rev. Lett. 93 (24) (2004) 243904.
[19] S. Mukherjee, L. Udpa, S. Udpa, E. J. Rothwell, Target localization using microwave time-reversal mirror in reflection mode, IEEE Transactions on Antennas and Propagation 65 (2) (2017) 820–828.
[20] Y. Deng, X. Liu, Electromagnetic imaging methods for nondestructive evaluation applications, Sensors 11 (12) (2011) 11774–11808.
[21] P. Blomgren, G. Papanicolaou, H. Zhao, Super-resolution in time-reversal acoustics, The Journal of the Acoustical Society of America 111 (1) (2002) 230–248.
[22] G. Papanicolaou, K. Solna, L. Ryzhik, Statistical stability in time reversal, SIAM Journal on Applied Mathematics 64 (4) (2004) 1133–1155.
[23] M. E. Yavuz, F. L. Teixeira, A numerical study of time-reversed uwb electromagnetic waves in continuous random media, IEEE Antennas and Wireless Propagation Letters 4 (2005) 43–46.
[24] I. El Baba, S. Lallechere, P. Bonnet, Electromagnetic time-reversal for reverberation chamber applications using fdtd, in: 2009 International Conference on Advances in Computational Tools for Engineering Applications, IEEE, 2009, pp. 157–162.
[25] M. E. Yavuz, Time reversal based signal processing techniques for ultrawideband electromagnetic sensing in random media, Ph.D. thesis, The Ohio State University (2007).
[26] J. De Rosny, G. Lerosey, M. Fink, Theory of electromagnetic time-reversal mirrors, IEEE Trans. Antennas Propag. 58 (10) (2010) 3139–3149.
[27] S. Mukherjee, A. Tamburrino, L. Udpa, S. Udpa, Nde of composite structures using microwave time reversal imaging, in: 42nd Annual Review of Progress in Quantitative Nondestructive Evaluation, Vol. 1706, AIP Publishing, 2016, p. 100002.
[28] K. Yee, Numerical solution of initial boundary value problems involving maxwell's equations in isotropic media, IEEE Transactions on antennas and propagation 14 (3) (1966) 302–307.
[29] B. R. Crowgey, E. J. Rothwell, L. C. Kempel, E. L. Mokole, Comparison of uwb short-pulse and stepped-frequency radar systems for imaging through barriers, Prog Electromagn Res 110 (2010) 403–419.
[30] S. Mukherjee, L. Udpa, Y. Deng, P. Chahal, E. J. Rothwell, Design of a microwave time reversal mirror for imaging applications, Progress In Electromagnetics Research C 77 (2017) 155–165.

Journal Pre-proof

Journal Pre-proof

Declaration of interests

☒ The authors declare that they have no known competing financial interests or personal relationships that could have appeared to influence the work reported in this paper.

☐The authors declare the following financial interests/personal relationships which may be considered as potential competing interests:

Jou rnal Pre-